Computational Materials Science 224 (2023) 112157

Contents lists available at ScienceDirect

Computational Materials Science

journal homepage: www.elsevier.com/locate/commatsci

Full length article

Coupling stress fields and vacancy diffusion in phase-field models of voids as pure vacancy phase

Kevin A. Pendl *, Thomas Hochrainer

Technische Universität Graz, Institut für Festigkeitslehre, Kopernikusgasse 24, 8010 Graz, Austria

ARTICLE INFO

Keywords:
Phase-field method
Elasto-diffusional model
Point defects
Voids
Small-strain elasticity

ABSTRACT

High vacancy concentrations in crystals may lead to formation and growth of voids, which is connected to swelling under irradiation and degradation of material properties. Recent experimental work suggests that vacancy condensation may also be involved in nucleation and evolution of porosity in early stages of ductile fracture. Mostly in the realm of irradiation effects, void formation and growth has been simulated with phase-field methods, where voids are treated as pure vacancy phases. Since vacancies induce an eigenstrain field, it is well-known that the evolution of vacancy concentrations is coupled to the elastic stress field. However, the few existing elastically coupled diffuse interface models of void growth seem to face a conceptual problem in the diffuse interface; in the center of which they predict the highest eigenstrains, which results in unrealistically high, fluctuating stresses. In the current work, we present a new model for coupling elastically driven vacancy diffusion with a diffuse interface model of void surfaces, which overcomes the named short-comings and closely reproduces the sharp interface solution. This is achieved by making the eigenstrain a function of the non-conserved order parameter used to distinguish the crystal and void phase. The model is verified for two-dimensional example problems by comparison to the analytical solution of the according sharp interface model. Eventually, the model is used to show the impact of elasto-diffusional coupling on void growth in mechanically loaded systems. We analyze the model with regard to the bi-stable energy landscape and discuss limitations and future prospects of the approach.

1. Introduction

High concentrations of vacancies in crystals as resulting from irradiation [1] or large plastic deformations [2,3] may lead to void formation and growth. Void condensation from vacancy supersaturation and subsequent void growth are well-known to be coupled to the phenomenon of swelling of irradiated materials [4,5] and they have recently been suggested to likewise play an important role in early stages of ductile failure [6,7]. Vacancy condensation and subsequent void growth have long been modeled in the realm of irradiation; classically in the spatially homogenized so-called 'rate theories' of microstructure evolution, but also in spatially resolved diffuse interface models using the phase-field method. The phase-field method (see, e.g. [8] or [9]) in this realm is essentially used to circumvent explicit interface tracking (or generation) and as a natural nucleation model for voids. The available phase-field models usually target microstructure evolution under irradiation and are not coupled to the stress field, although stress is known to be coupled to point defect diffusion. Exceptions are found in [10–14] and in the works of Yu and Lu, [15,16], where anisotropic elastic effects where put forth as explanation for distinct types of void lattices observed in crystals of different symmetry classes. If void nucleation and growth shall be considered in the realm of ductile fracture, a proper coupling of phase-field models of vacancy concentration to elasticity is mandatory.

Coupling of stress and vacancy kinetics is well known to result from the eigenstrain of vacancies which emerges from the relaxation of the surrounding crystal lattice if a single atom is removed. In continuum formulations, the eigenstrain field of a vacancy distribution is usually modeled to be proportional to the vacancy concentration. However, combining the vacancy concentration-based eigenstrain formulation with the phase-field description of voids as a pure vacancy phase faces a conceptual problem in the interface, where the vacancy concentration is ≈ 0.5 while the elastic constants, which are commonly interpolated between crystal and void phase, are likewise about half of those of the considered crystal (see next paragraph for details). The resulting huge and strongly varying eigenstrain in the interface consequently causes large stresses in and across the interface, which are usually not in accordance with stresses in corresponding sharp interface models.

* Corresponding author.
E-mail address: kevin.pendl@tugraz.at (K.A. Pendl).

https://doi.org/10.1016/j.commatsci.2023.112157
Received 3 February 2023; Received in revised form 21 March 2023; Accepted 24 March 2023
Available online 13 April 2023

In the latter models, void surfaces are usually considered as stress-free or, in the case of gas filled bubbles, subject to pressure boundary conditions. In the current work we propose a formulation for coupling elastically driven vacancy diffusion with a diffuse interface model of void surfaces, which strongly alleviates the occurring stresses in the void surface as compared to existing models.

Phase-field models of void formation and growth from vacancy supersaturation fall into two categories, in that either the vacancy concentration c^{v} is at the same time the indicator of crystal ($c^{\mathrm{v}} = c^{\mathrm{v}}_{\mathrm{eq}}$ or $c^{\mathrm{v}} = 0$, since the equilibrium vacancy concentration is very small, $c^{\mathrm{v}}_{\mathrm{eq}} \ll 1$) or void phase ($c^{\mathrm{v}} = 1$), e.g. [15–17]; or such that an additional, non-conserved order parameter, called η in the sequel, is used to indicate the phases, where the energy is such that the vacancy concentration tries to assume the above named values in the according phases [10,18–20]. The latter kind of models have been put forth by El-Azab and co-workers [21–23] who corroborated the feasibility of this approach by asymptotic matching with a sharp interface model [24] allowing for distinct point defect reaction kinetics at the surface [25]. In the current work, we adopt an approach with an additional order parameter η, which turns out to be likewise crucial for the stress coupling at void surfaces.

As for coupling the vacancy based phase-field models with stresses, two aspects need to be modeled. On the one hand, the combination of void and crystal phase requires modeling the elastic properties of the phases and, across the interface where both phases formally overlap, an interpolation of the elastic properties and/or the distribution of stress or strain among the two phases. This homogenization problem has been discussed in detail in [26] for phase-field models of two solid phases. In the phase-field literature, the most widely applied interpolation scheme in the overlap region is Khachaturyan's (compare e.g. [27–29]), where the elastic stiffness tensor $\mathbb{C}$ and the eigenstrain tensor $\boldsymbol{\varepsilon}^*$ are interpolated between the phases. As for the homogenization of the elastic properties, we adopt this model in the current work. On the other hand, the eigenstrain field in the bulk due to vacancies is modeled as a function of the vacancy concentration. In sharp interface models, the eigenstrain is usually considered as linear function of the vacancy concentration $\boldsymbol{\varepsilon}^*(c^{\mathrm{v}}) \propto c^{\mathrm{v}}\boldsymbol{\varepsilon}^{\mathrm{v}}$, where $\boldsymbol{\varepsilon}^{\mathrm{v}}$ denotes the eigenstrain of a single vacancy. If the vacancy eigenstrain is isotropic, i.e. $\boldsymbol{\varepsilon}^{\mathrm{v}} = \varepsilon^{\mathrm{v}}/3\,\mathbf{I}$ with a volumetric scalar eigenstrain ε^{v} and the unit matrix $\mathbf{I}$, this yields driving forces for drift diffusion proportional to the gradient of the hydrostatic pressure. Though the proportionality of the eigenstrain field to the concentration is only valid for relatively low vacancy concentrations and thus questionable for the values reached in phase-field models across the interface and in the void, it is also sometimes used in diffuse interface models, e.g. in [18,30]. In phase-field models based solely on the vacancy concentration, the fact that vacancies do not have eigenstrain in the void phase may be accounted for by the quadratic form $\boldsymbol{\varepsilon}^*(c^{\mathrm{v}}) = c^{\mathrm{v}}(1 - c^{\mathrm{v}})\boldsymbol{\varepsilon}^{\mathrm{v}}$, as done e.g. in [13–16,31,32]. This form may also be viewed as an interpolation (homogenization) of the eigenstrain of vacancies in either 'phase' as will be explained in more detail towards the end of in Section 2. However, in modeling voids, this makes the eigenstrain maximal for $c^{\mathrm{v}} = 0.5$, i.e. at the nominal position of the interface. While Yu and Lu, [15,16], consider this as asset accounting for misfit stress in the interface, it seems questionable why these eigenstrains should be isotropic in the interface and why their strength is modeled with the same relaxation strain as for vacancies in the bulk. We note that whether and to which extent this affects the results of the named papers is not known to the present authors.

This paper is structured such that in the subsequent Section 2 we introduce the governing equations of the phase-field model and briefly discuss its numerical implementation in Section 3. The determination of the order parameter dependent equilibrium vacancy concentration is explained in Section 4. The simulation results obtained with two different eigenstrain formulations are presented in Section 5, which is followed by a discussion and an analysis of the model by means of the bi-stable energy landscape in Section 6. Eventually, we provide conclusions from the work in Section 7.

2. Model formulation

The employed phase-field model is based on the work of Rokkam et al. [19,21,22,33], who investigated the evolution of voids due to the coupled evolution of vacancies and (self-)interstitial atoms under irradiation. For the current work we only adopt the vacancy related part of the model, since our intention is directed rather towards void formation during plastic deformation than during irradiation. Under irradiation, the high energies of impacting particles lead to an atomic displacement cascade which produces interstitial atoms and vacancies roughly in the same amount. The annihilation bias of point defect sinks, e.g. grain boundaries and dislocations, and the high diffusivity of interstitial atoms explains the ensuing high vacancy supersaturations leading to void formation. However, during plastic deformation there is a production bias of the processes which generate point defects, for instance, by non-conservative motion of dislocation jogs [34]. Due to their lower formation energy, vacancies are generated far more easily than interstitial atoms, which is why we do not model the latter in the current work. Note though, that the method developed for incorporating elastic effects is expected to be transferable to coupled models including interstitials.

We consider a single-component crystalline material that can exist in two stable phases: a bulk material region in which single vacancies diffuse and a void region defined as a pure vacancy phase. The phase distinction is done by a non-conserved order parameter η. Due to the underlying phase-field description, the two phases are separated by a diffuse interface in which the order parameter and the vacancy concentration c^{v} vary continuously between their equilibrium values (bulk: $c^{\mathrm{v}} = c^{\mathrm{v}}_{\mathrm{eq}}$, $\eta = 0$; void: $c^{\mathrm{v}} = \eta = 1$). The two variables are coupled via the eigenstrain field $\boldsymbol{\varepsilon}^*(c^{\mathrm{v}}, \eta)$ to an elastic strain field $\boldsymbol{\varepsilon}^{\mathrm{el}}$ to investigate elasto-diffusional behavior. The constitutive model is specified by an energy functional $\Psi\left[c^{\mathrm{v}}, \eta, \boldsymbol{\varepsilon}^{\mathrm{el}}\right]$, with the kinetic response and constitutive relationships for the primary variables being derived from the balance laws for entropy, species concentrations, linear momentum and moment of momentum by the standard procedure of Coleman and Noll [35]. The resulting coupled system of equations reads,

$$\partial_t c^{\mathrm{v}} = \boldsymbol{\nabla} \cdot M \boldsymbol{\nabla} \left(\frac{\delta \Psi}{\delta c^{\mathrm{v}}} \right) \quad \text{in } \Omega\,, \tag{2.1a}$$

$$\partial_t \eta = -L \frac{\delta \Psi}{\delta \eta} \quad \text{in } \Omega\,, \tag{2.1b}$$

$$\boldsymbol{\sigma} = \frac{\delta \Psi}{\delta \boldsymbol{\varepsilon}^{\mathrm{el}}}\,, \tag{2.1c}$$

$$\boldsymbol{\nabla} \cdot \boldsymbol{\sigma} = \mathbf{0} \quad \text{in } \Omega\,, \tag{2.1d}$$

with δ indicating functional derivatives and the del operator $\boldsymbol{\nabla}$ denoting the material gradient and $\boldsymbol{\nabla}\cdot$ the according divergence operator. Eq. (2.1a) is the (modified) Cahn–Hilliard equation, which results from the species balance of vacancies and describes the evolution of the vacancy concentration. The gradient of the functional derivative with respect to the concentration defines the driving force for vacancy diffusion and M is the vacancy mobility which is specified below. Eq. (2.1b) is the Allen–Cahn equation, which defines the evolution of the order parameter η, where the functional derivative of the free energy with respect to the order parameter is a generalized driving force for void evolution and L is a generalized surface mobility. The stress tensor $\boldsymbol{\sigma}$ emerges as the variational derivative of the energy density with respect to the elastic strain, Eq. (2.1c), and Eq. (2.1d) represents the mechanical equilibrium with vanishing body forces. Moreover, balance of moment of momentum requires the stress tensor to be symmetric, i.e. $\boldsymbol{\sigma}^{\mathrm{T}} = \boldsymbol{\sigma}$. Boundary conditions vary in the applications below and include displacement and traction boundary conditions for the elastic problem. For the order parameter and the vacancy concentration we employ no-flux boundary conditions in the applications below.

Within phase-field modeling, the total free energy density is expressed in terms of the free energy densities of its constituent phases and interfaces [36–38]. We define the total free energy Ψ of the

observed system as an energy functional that depends on the fields of vacancy concentration, order parameter, and the elastic strain tensor via integration of a local energy density ψ as

$$\Psi := \Psi\left[c^{\mathrm{v}}, \eta, \boldsymbol{\varepsilon}^{\mathrm{el}}\right] = \int_{\Omega} \psi \,\mathrm{d}V = \int_{\Omega} \left(\psi^{\mathrm{hom}}(c^{\mathrm{v}}, \eta) + \psi^{\mathrm{gr}}(\boldsymbol{\nabla} c^{\mathrm{v}}, \boldsymbol{\nabla}\eta) + \psi^{\mathrm{el}}(c^{\mathrm{v}}, \eta, \boldsymbol{\varepsilon}^{\mathrm{el}})\right) \mathrm{d}V. \tag{2.2}$$

The energy density is assumed to be expressible as the sum of several energy density contributions which depend on the underlying fields or their derivatives. The first energy density contribution inside the integral describes the free energy density of a (would-be) homogeneous system based on the local vacancy concentration and the order parameter [33]:

$$\psi^{\mathrm{hom}}(c^{\mathrm{v}}, \eta) = \frac{1}{\Omega^{\mathrm{a}}}\left[(1-h(\eta))\left(\psi^{\mathrm{bulk}}(c^{\mathrm{v}}) - \psi^{\mathrm{ref}}\right) + w(c^{\mathrm{v}}, \eta)\right], \tag{2.3}$$

where Ω^{a} is the atomic volume. The bulk free energy density $\psi^{\mathrm{bulk}}(c^{\mathrm{v}})$ in units of energy per lattice site is taken to be of the form $\psi^{\mathrm{bulk}}(c^{\mathrm{v}}) = (E_{\mathrm{f}}^{\mathrm{v}} - T s_{\mathrm{f}}^{\mathrm{v}})\, c^{\mathrm{v}} + k_{\mathrm{B}} T\left[c^{\mathrm{v}} \ln c^{\mathrm{v}} + (1-c^{\mathrm{v}}) \ln(1-c^{\mathrm{v}})\right]$. The reference energy density ψ^{ref} is determined from requiring that for the equilibrium concentration $c^{\mathrm{v}} = c_{\mathrm{eq}}^{\mathrm{v}}$ in the bulk, the homogeneous energy densities of the bulk and the void phase are equal, i.e. $\psi^{\mathrm{hom}}(c^{\mathrm{v}} = c_{\mathrm{eq}}^{\mathrm{v}}, \eta = 0) \overset{!}{=} \psi^{\mathrm{hom}}(c^{\mathrm{v}} = 1, \eta = 1)$. The function $h(\eta) = \eta^3(6\eta^2 - 15\eta + 10)$ varies monotonously from $h(\eta = 0) = 0$ to $h(\eta = 1) = 1$. The parameters in the bulk free energy density are the formation energy $E_{\mathrm{f}}^{\mathrm{v}}$ and formation entropy $s_{\mathrm{f}}^{\mathrm{v}}$ of vacancies in the bulk material, the Boltzmann constant k_{B} and absolute temperature T. The thermal equilibrium vacancy concentration is given by $c_{\mathrm{eq}}^{\mathrm{v}} = 1/(1+\exp C)$, with $C = \left(E_{\mathrm{f}}^{\mathrm{v}} - T s_{\mathrm{f}}^{\mathrm{v}}\right)/\left(k_{\mathrm{B}} T\right)$, as results from requiring the stable phases to be extremal points of the homogeneous energy, i.e. from solving $\partial_{c^{\mathrm{v}}}(\psi^{\mathrm{hom}})\big|_{c^{\mathrm{v}}=c_{\mathrm{eq}}^{\mathrm{v}},\eta=0} = 0$ for the concentration. The so-called Landau energy $w(c^{\mathrm{v}}, \eta) = \bar{w}\left((c^{\mathrm{v}}-1)^2\eta^2 + (c^{\mathrm{v}} - c_{\mathrm{eq}}^{\mathrm{v}})^2(\eta-1)^2\right)$ is responsible for the bi-stability in the system, where the constant $\bar{w}$ defines the height of the energy barrier between the two phases. The Landau term is defined such that it adheres to thermodynamic restrictions regarding the minima of the bulk and void phase, cf. [33]. The gradient energy density ψ^{gr} is chosen as usual in diffuse interface approaches,

$$\psi^{\mathrm{gr}}(\boldsymbol{\nabla} c^{\mathrm{v}}, \boldsymbol{\nabla}\eta) = \frac{1}{\Omega^{\mathrm{a}}}\left[\frac{\kappa^{\mathrm{c}}}{2}|\boldsymbol{\nabla} c^{\mathrm{v}}|^2 + \frac{\kappa^{\eta}}{2}|\boldsymbol{\nabla}\eta|^2\right], \tag{2.4}$$

where κ^{c} and κ^{η} are the gradient energy coefficients characterizing the energy penalties corresponding to the inhomogeneities in the vacancy concentration and the order parameter. The long-range interaction, i.e. the elastic response of the system under consideration, is modeled with the elastic energy density

$$\psi^{\mathrm{el}}(c^{\mathrm{v}}, \eta, \boldsymbol{\varepsilon}^{\mathrm{el}}) = \frac{1}{2}\boldsymbol{\varepsilon}^{\mathrm{el}}(c^{\mathrm{v}}, \eta) : \mathbb{C}(\eta) : \boldsymbol{\varepsilon}^{\mathrm{el}}(c^{\mathrm{v}}, \eta), \tag{2.5}$$

with the fourth-order elasticity tensor $\mathbb{C}(\eta) = (1-h(\eta))\,\mathbb{C}^{\mathrm{bulk}}$ being a function of the order parameter. Here, $\mathbb{C}^{\mathrm{bulk}}$ denotes the elasticity tensor of the bulk material and $\boldsymbol{\varepsilon}^{\mathrm{el}}(c^{\mathrm{v}}, \eta)$ is the elastic small-strain tensor, i.e. the difference of the total strain and the eigenstrain, $\boldsymbol{\varepsilon}^{\mathrm{el}}(c^{\mathrm{v}}, \eta) = \boldsymbol{\varepsilon} - \boldsymbol{\varepsilon}^{*}(c^{\mathrm{v}}, \eta)$. In the current work we employ isotropic elasticity, such that the elasticity tensor assumes the form $\mathbb{C}^{\mathrm{bulk}} = K\,\mathbf{I}\otimes\mathbf{I} + G(\mathbb{I} - 2/3\,\mathbf{I}\otimes\mathbf{I})$, where K and G are bulk and shear modulus, respectively, $\mathbf{I}$ is the unit matrix and $\mathbb{I}$ denotes the fourth order identity tensor on the space of symmetric tensors.

If the formulation of the total free energy, Eq. (2.2), is inserted in Eq. (2.1), one obtains the kinetic equations of the underlying coupled Cahn–Hilliard & Allen–Cahn model (compare [39]) as well as the stress tensor as

$$\partial_t c^{\mathrm{v}} = \boldsymbol{\nabla}\cdot M\,\boldsymbol{\nabla}\left[\partial_{c^{\mathrm{v}}}(\psi^{\mathrm{hom}} + \psi^{\mathrm{el}}) - \frac{\kappa^{\mathrm{c}}}{\Omega^{\mathrm{a}}}\boldsymbol{\nabla}^2 c^{\mathrm{v}}\right], \tag{2.6a}$$

$$\partial_t \eta = -L\left[\partial_{\eta}(\psi^{\mathrm{hom}} + \psi^{\mathrm{el}}) - \frac{\kappa^{\eta}}{\Omega^{\mathrm{a}}}\boldsymbol{\nabla}^2\eta\right], \tag{2.6b}$$

$$\boldsymbol{\sigma} = \mathbb{C}(\eta) : \boldsymbol{\varepsilon}^{\mathrm{el}}(c^{\mathrm{v}}, \eta). \tag{2.6c}$$

The vacancy mobility M is of degenerate character, i.e., it depends on the vacancy concentration, $M(c^{\mathrm{v}}) = \Omega^{\mathrm{a}} D\, c^{\mathrm{v}}(1-c^{\mathrm{v}})/(k_{\mathrm{B}}T)$ with D being the vacancy diffusivity. In conjunction with only the homogeneous energy density, Eq. (2.3), this form of the mobility reproduces Fickian diffusion in the bulk ($\eta = 0$).

For the eigenstrain we oppose two different approaches, namely

$$\boldsymbol{\varepsilon}^{*}(c^{\mathrm{v}}, \eta) = \left(c^{\mathrm{v}} - c_{\mathrm{eq}}^{\mathrm{v}}\right)(1-h(\eta))\,\boldsymbol{\varepsilon}^{\mathrm{v}} \tag{2.7}$$

and

$$\boldsymbol{\varepsilon}^{*}(c^{\mathrm{v}}, \eta) = \left(c^{\mathrm{v}} - c_{\mathrm{eq}}^{\mathrm{v}}(\eta)\right)\boldsymbol{\varepsilon}^{\mathrm{v}}, \tag{2.8}$$

which we refer to in following as the *interpolation* and *equilibrium profile* approach, respectively. The interpolation approach, Eq. (2.7), follows a description similar to other phase-field models for coupled elasto-diffusional evolution described with Cahn–Hilliard-type phase-field models, e.g. [15,31], where the eigenstrain is a quadratic function of the concentration, $\boldsymbol{\varepsilon}^{*}(c^{\mathrm{v}}) = c^{\mathrm{v}}(1-c^{\mathrm{v}})\boldsymbol{\varepsilon}^{\mathrm{v}}$. The reason we call this type of models 'interpolation' approach is that we may define a (vanishing) vacancy eigenstrain *in the void* as $\boldsymbol{\varepsilon}_{\mathrm{void}}^{\mathrm{v}} = 0$. An interpolated vacancy eigenstrain $\bar{\boldsymbol{\varepsilon}}^{\mathrm{v}}$ between the phase dependent eigenstrains of the vacancies is accordingly defined in models solely based on the concentration as

$$\bar{\boldsymbol{\varepsilon}}^{\mathrm{v}}(c^{\mathrm{v}}) = (1-c^{\mathrm{v}})\boldsymbol{\varepsilon}^{\mathrm{v}} + c^{\mathrm{v}}\boldsymbol{\varepsilon}_{\mathrm{void}}^{\mathrm{v}} = (1-c^{\mathrm{v}})\boldsymbol{\varepsilon}^{\mathrm{v}}, \tag{2.9}$$

and in the current case as

$$\bar{\boldsymbol{\varepsilon}}^{\mathrm{v}}(\eta) = (1-h(\eta))\boldsymbol{\varepsilon}^{\mathrm{v}} + h(\eta)\boldsymbol{\varepsilon}_{\mathrm{void}}^{\mathrm{v}} = (1-h(\eta))\boldsymbol{\varepsilon}^{\mathrm{v}}. \tag{2.10}$$

The interpolation approach from the literature thus reads $\boldsymbol{\varepsilon}^{*}(c^{\mathrm{v}}) = c^{\mathrm{v}}\bar{\boldsymbol{\varepsilon}}^{\mathrm{v}}(c^{\mathrm{v}})$ and the one in the current work reads $\boldsymbol{\varepsilon}^{*}(c^{\mathrm{v}}, \eta) = \left(c^{\mathrm{v}} - c_{\mathrm{eq}}^{\mathrm{v}}\right)\bar{\boldsymbol{\varepsilon}}^{\mathrm{v}}(\eta)$.

For both interpolation approaches the eigenstrain attains its maximum somewhere in the middle of the diffuse interface. As we shall see in Section 5, for the current variant (2.7) this leads to high stresses and stress fluctuations within the interface. Such stresses appear unrealistic since free interfaces in mechanically unloaded systems would be assumed stress-free. We also note that when regarding the definition $\boldsymbol{\varepsilon}^{*}(c^{\mathrm{v}}, \eta) = \left(c^{\mathrm{v}} - c_{\mathrm{eq}}^{\mathrm{v}}\right)\bar{\boldsymbol{\varepsilon}}^{\mathrm{v}}(\eta)$, there arises the questions why we would consider the difference between the vacancy concentration and the equilibrium vacancy concentration *in the bulk* to also be of relevance in the void; note that the 'equilibrium' vacancy concentration in the void is in fact $c^{\mathrm{v}} = 1$.

In the equilibrium profile approach (2.8) we take up this line of thought and define an η-dependent equilibrium concentration, $c_{\mathrm{eq}}^{\mathrm{v}}(\eta)$. This relation is obtained from the equilibrated common distributions of c^{v} and η across a flat diffuse interface. In this way, when the elastic energy is added, a flat equilibrated surface between a void and a crystal with equilibrium concentration in the bulk will be free of eigenstrains and thus also of stresses. Note that in this approach we allow for non-trivial eigenstrains in the void when c^{v} is not exactly equal to one, but this does not lead to noticeable stresses because of the interpolated elasticity tensor $\mathbb{C}(\eta)$, which nearly vanishes where $\eta \approx 1$, i.e. in the void. Further details on the identification and definition of the functional dependence $c_{\mathrm{eq}}^{\mathrm{v}}(\eta)$ will be provided in Section 4 and a detailed interpretation of this functional dependence is put forth in the Discussion, Section 6.

3. Methods

The governing equations are brought into a dimensionless form by using a suitable transformation of time ($t \to \tau\tilde{t}$), space ($\boldsymbol{x} \to \xi\tilde{\boldsymbol{x}}$), temperature ($T \to \Theta\tilde{T}$) and energy density ($\psi \to \epsilon\tilde{\psi}$), with τ, ξ, Θ and ϵ being the respective characteristic scales, compare e.g. [39]. Following an analogous approach to [33], upon choosing a length scale ξ, a suitable time scale τ is defined as $\tau := \xi^2/D$. For example, if $\xi = 1\,\mathrm{nm}$, the time scale for a simulation temperature of $T =$

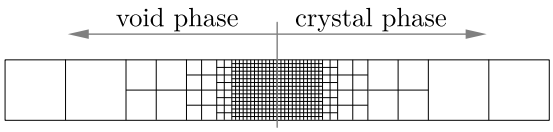

Fig. 1. Mesh of slab geometry to obtain parameters of $c^{\mathrm{v}}_{\mathrm{eq}}(\eta)$ with indication of the phase distribution.

1000 K is $\tau = 0.1701\,\mathrm{ns}$, where $D = D_0 \exp\left(-E^{\mathrm{v}}_{\mathrm{m}}/(k_{\mathrm{B}}T)\right)$ with the pre-exponential factor $D_0 = 0.25\,\mathrm{cm}^2/\mathrm{s}$ and the migration energy of vacancies $E^{\mathrm{v}}_{\mathrm{m}} = 0.72\,\mathrm{eV}$ [40]. We take the characteristic temperature to be the melting temperature of the bulk, i.e. $\Theta := T_{\mathrm{melt}}$, and the energy densities and likewise stresses and elastic constants are scaled with $\epsilon := k_{\mathrm{B}}\Theta/\Omega^{\mathrm{a}}$. After incorporating the degenerate mobility and applying the non-dimensionalization, the governing equations read

$$\partial_{\tilde{t}} c^{\mathrm{v}} = \frac{1}{\tilde{T}}\tilde{\boldsymbol{\nabla}}\cdot\left\{c^{\mathrm{v}}(1-c^{\mathrm{v}})\tilde{\boldsymbol{\nabla}}\left[\partial_{c^{\mathrm{v}}}(\tilde{\psi}^{\mathrm{hom}}+\tilde{\psi}^{\mathrm{el}}) - \tilde{\kappa}^{\mathrm{c}}\tilde{\boldsymbol{\nabla}}^2 c^{\mathrm{v}}\right]\right\} \quad \text{in } \Omega\,, \tag{3.1a}$$

$$\partial_{\tilde{t}}\eta = -\tilde{L}\left[\partial_{\eta}(\tilde{\psi}^{\mathrm{hom}}+\tilde{\psi}^{\mathrm{el}}) - \tilde{\kappa}^{\eta}\tilde{\boldsymbol{\nabla}}^2\eta\right] \quad \text{in } \Omega\,, \tag{3.1b}$$

$$\tilde{\boldsymbol{\sigma}} = \tilde{\mathbb{C}}(\eta) : \boldsymbol{\varepsilon}^{\mathrm{el}}(c^{\mathrm{v}}, \eta)\,, \tag{3.1c}$$

$$\tilde{\boldsymbol{\nabla}}\cdot\tilde{\boldsymbol{\sigma}} = \mathbf{0} \quad \text{in } \Omega\,, \tag{3.1d}$$

where the tilde $(\tilde{.})$ indicates dimensionless quantities and operators. The dimensionless generalized surface mobility $\tilde{L}$ as well as the dimensionless gradient energy coefficients, i.e. $\tilde{\kappa}^{\mathrm{c}}$ and $\tilde{\kappa}^{\eta}$, are defined through

$$\tilde{L} := L\,\tau\,\epsilon, \quad \tilde{\kappa}^{\mathrm{c}} := \frac{\kappa^{\mathrm{c}}}{\Omega^{\mathrm{a}}\,\xi^2\,\epsilon}, \quad \tilde{\kappa}^{\eta} := \frac{\kappa^{\eta}}{\Omega^{\mathrm{a}}\,\xi^2\,\epsilon}. \tag{3.2}$$

Since reliable experimental data for the mobility L and the gradient energy coefficients κ^{c} and κ^{η} is not available, they are chosen such that the model can reproduce the envisaged physical phenomena. The employed values are provided in Table 1.

Eqs. (3.1) are implemented in the phase-field framework PRISMS-PF [41], a parallel finite element code for conducting simulations related to microstructural evolution. The spatial discretization is realized with linear Gauss–Lobatto elements, where the quadrature points coincide with the element nodes. Explicit time-stepping is used for time discretization. We assume the relaxation dynamics for elasticity to be much faster than for the diffusion of the vacancy concentration and the order parameter. Accordingly, we solve the mechanical equilibrium, Eq. (3.1d), for the current phase fields at each time step. In PRISMS-PF this is conducted by using the conjugate gradient scheme [41].

Note that in the current work we perform two-dimensional simulations in plane-strain. This leaves the symbolic form of the equations unchanged and the components of the elasticity tensor for plane-strain are just the two-dimensional subset of the full tensor. It seems worth noting, though, that the plane-strain assumptions requires using plane eigenstrains which means that for plane-strain in the 1–2-plane we use the vacancy eigenstrain

$$\boldsymbol{\varepsilon}^{\mathrm{v}} = \frac{\varepsilon^{\mathrm{v}}}{2}\left(\mathbf{I} - \boldsymbol{e}_3\otimes\boldsymbol{e}_3\right), \tag{3.3}$$

where $\boldsymbol{e}_3$ denotes the unit vector in the normal direction to the plane.

4. Identification of the equilibrium profile

We developed the equilibrium profile approach (2.8) under the premise that an equilibrated flat surface should be stress-free. To this end we first determined the equilibrium profiles of c^{v} and η for the phase-field model without the elastic energy contribution. For the equilibration we initialized both parameter fields with a tanh-profile across a flat, free surface (to a void region) of a material with equilibrium vacancy concentration $c^{\mathrm{v}}_{\mathrm{eq}}$ in the bulk. The simulation domain of 72×8 dimensionless length units squared was discretized with 444 elements, compare Fig. 1, and the dimensionless time step was chosen to be $\Delta\tilde{t} = 10^{-4}$. To ensure an equilibrium state, the simulation was performed till the change of total free energy of the system between two time steps n and $n+1$, compared to the initial total energy Ψ^0 at $t=0$, was negligible, i.e., when $(\Psi^{n+1}-\Psi^n)/\Psi^0 < 10^{-10}$. The equilibrated profiles of c^{v} and η are displayed in Fig. 2 (b), where the void is on the left and the crystal on the right hand side of the displayed section. Based on these profiles we plotted the c^{v} values over the values of the order parameter η across the interface which yields the curve displayed in Fig. 2 (a). The graph suggested a functional relationship of the form

$$c^{\mathrm{v}}_{\mathrm{eq}}(\eta) = p_1\exp(-p_2/\eta^{p_3}) + p_4\,\eta^{p_5} + c^{\mathrm{v}}_{\mathrm{eq}}, \tag{4.1}$$

with fitting parameters p_1 to p_5. Fitting was conducted using the function `curve_fit` of the submodule namespace `scipy.optimize` in Python [42,43]. Employing `curve_fit`, a non-linear least squares method is used to fit a predefined function to the provided data by giving an initial guess for the sought parameters. The initial guess was set to $p_i = 1, i \in \{1,\dots,5\}$, for which we achieved very good fits upon convergence. For the chosen simulation parameters, cf. Table 1, we obtained the parameters such that

$$c^{\mathrm{v}}_{\mathrm{eq}}(\eta) = 1.499\exp(-0.917/\eta^{0.826}) + 0.400\,\eta^{3.793} + c^{\mathrm{v}}_{\mathrm{eq}}. \tag{4.2}$$

Fig. 2 (a) shows the simulation results as well as the fitted function of the relationship between vacancy concentration and order parameter. In Fig. 2 (b) we display besides the equilibrated profiles also the η-dependent $c^{\mathrm{v}}_{\mathrm{eq}}(\eta)$ as obtained from Eq. (4.2) applied to the η-profile. This 'phase-dependent' equilibrium vacancy concentration is used in the eigenstrain definition (2.8), such that the uncoupled equilibrium profiles at a flat surface of a material with equilibrium vacancy concentration is free of eigenstrain. In Section 6 we further analyze the obtained $c^{\mathrm{v}}_{\mathrm{eq}}(\eta)$-profile with regard to the bi-stable energy landscape of the phase-field formulation.

5. Results

For analyzing the stress fields predicted by the two models we place a single void with dimensionless radius $\tilde{r} = \tilde{r}_{\mathrm{void}}$ in the center of the domain, compare Fig. 3 left. The stresses are analyzed for two cases, (a) for a void in a material with thermal equilibrium concentration of vacancies ($S^{\mathrm{v}} = 1$) and (b) for a void in a material that is 50-times supersaturated with vacancies ($S^{\mathrm{v}} = 50$), where we introduced the value of supersaturation $S^{\mathrm{v}} = c^{\mathrm{v}}/c^{\mathrm{v}}_{\mathrm{eq}}$. Employing the symmetry of the problem, only a quarter of the domain is analyzed, with a side length of 200 dimensionless length units. The initial mesh is displayed on the right hand side of Fig. 3. No-flux boundary conditions are applied for the vacancy concentration c^{v} and the order parameter η at all boundaries. For the displacement, symmetric boundary conditions are applied at the symmetry planes, while the displacement in $\tilde{x}$- and $\tilde{y}$-direction is set to zero at the other boundaries, cf. central image in Fig. 3. The time step is chosen as $\Delta\tilde{t} = 10^{-4}$ in dimensionless time units. The model parameters of copper used for the calculations are listed in Table 1. The single void is initialized with a tanh-profile in radial direction both for vacancy concentration and order parameter if not stated otherwise. The simulations in the next Subsection are performed till the relative change of the total free energy was negligible, as described in Section 4.

5.1. Stress-field around a void in bulk material with thermal equilibrium vacancy concentration

To begin with, we discuss the reason for turning away from the interpolation approach. The stimulus for eigenstrains and thus internal stresses is the supersaturation. Hence, for $S^{\mathrm{v}} = 1$ the stresses at a flat surface should be zero. Though for a circular void (very) minor hoop stresses might be expected at the surface, since the equilibrium vacancy concentration is known to be slightly curvature dependent [24], the

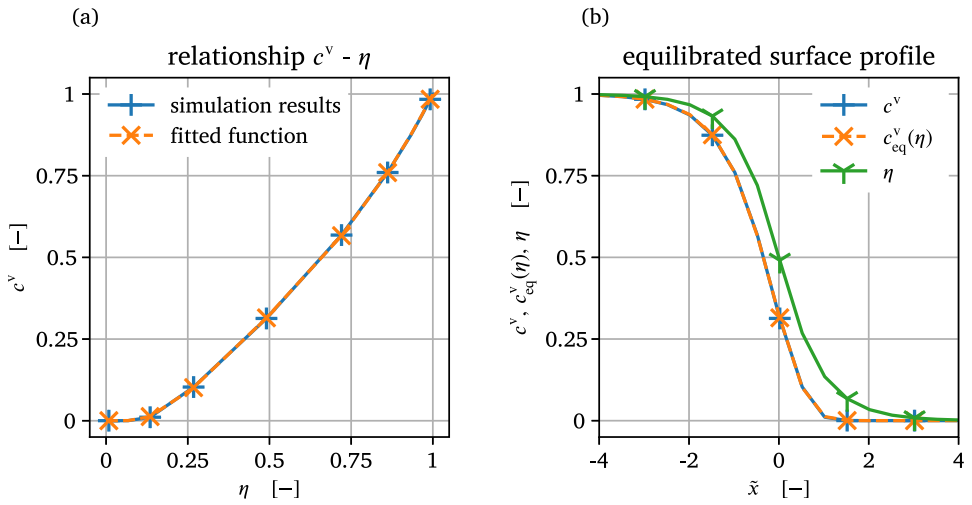

Fig. 2. Results of equilibration at flat surface: (a) functional relationship $c^v_{eq}(\eta)$, (b) equilibrium phase-field profiles.

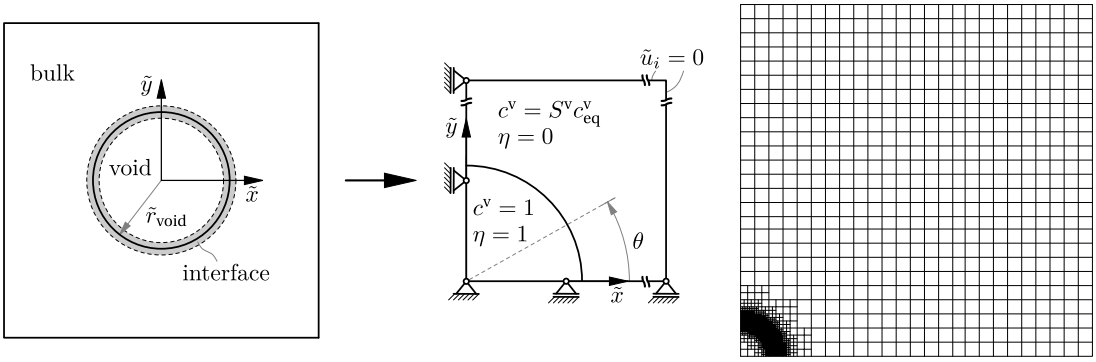

Fig. 3. Schematic representation of considered geometry with initial and boundary conditions (left and center) and the employed initial mesh (right).

Table 1
Model parameters used in the phase-field model simulations. In the unit column, ls stands for 'lattice site'.

Symbol	Parameter	Value	Unit	Reference
E^v_f	formation energy of vacancies	1	eV/ls	[33]
s^v_f	formation entropy of vacancies	$2.969\,k_B$	eV/(K ls)	[44]
Ω^a	atomic volume	1.182×10^{-29}	m^3	[45]
T_{melt}	melting temperature	1356	K	[45]
E	Young's modulus	130	GPa	[46]
ν	Poisson ratio	0.34	–	[46]
ε^v	volumetric eigenstrain	−0.2	–	[1]
k_B	Boltzmann constant	$8.617\,34 \times 10^{-5}$	eV/K	–
$\tilde{w}$	Landau prefactor	1	eV/ls	[33]
$\tilde{L}$	dimensionless generalized surface mobility	1	–	[33]
κ^η	gradient energy coefficient order parameter	$1.0\,\xi^2$	eV	[23]
κ^c	gradient energy coefficient vacancy concentration	$1.0\,\xi^2$	eV	[23]
T	simulation temperature	1000	K	–
$\tilde{r}_{void}$	dimensionless void radius	20	–	–

radial stresses still should be trivial at a curved free surface. However, for the interpolation approach we observe high stress peaks in the interface for hoop and radial stresses. In Fig. 4, plots of the radial and hoop stress as a function of the dimensionless distance to the void center ratio $\tilde{r}/\tilde{r}_{void}$ for two distinct directions, $\theta = 0°$ and $\theta = 45°$, are displayed. There is a slight discrepancy between the stresses along the two directions due to the discretization of a circular void with quadrilateral elements. However, along either direction one observes strong fluctuations and high peaks for the radial and hoop stress. The maximal eigenstrain is found near the nominal position of the void surface (at $\eta = 0.5$). As noted above, the high stresses within and their fluctuations across the diffuse interface are deemed non-physical. Moreover, besides the strong fluctuations within the diffuse interface, note that this model also predicts considerable stresses in the bulk close to the void surface, reaching values of about 55 MPa and −165 MPa for the radial and circumferential stresses, respectively (cf. Fig. 4). As opposed to the stresses within the surface, the bulk stresses are essentially independent of the direction chosen for evaluation.

As a remedy for the explained problem we propose considering the equilibrium vacancy concentration to be a function of the order parameter, i.e. Eq. (2.8). The stresses obtained from the equilibrium profile approach with identical simulation parameters and initial conditions to those in the interpolation approach are displayed in Fig. 5. Here, too, the radial and hoop stress show peaks at $\tilde{r} \approx \tilde{r}_{void}$, but the stresses are an order of magnitude smaller than those of the interpolation approach. Likewise, the radial and circumferential stresses in the bulk close to

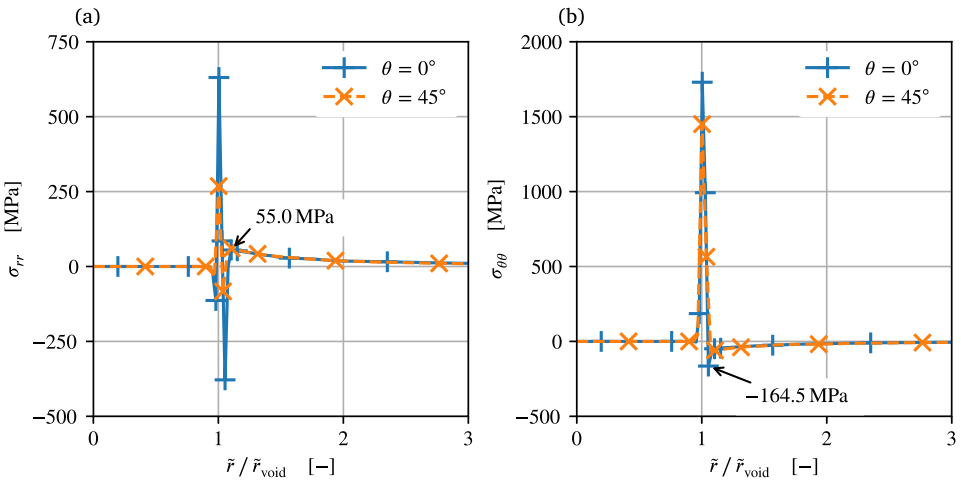

Fig. 4. Radial stress (a) and hoop stress (b) near a void in material without supersaturation as obtained from the interpolation approach.

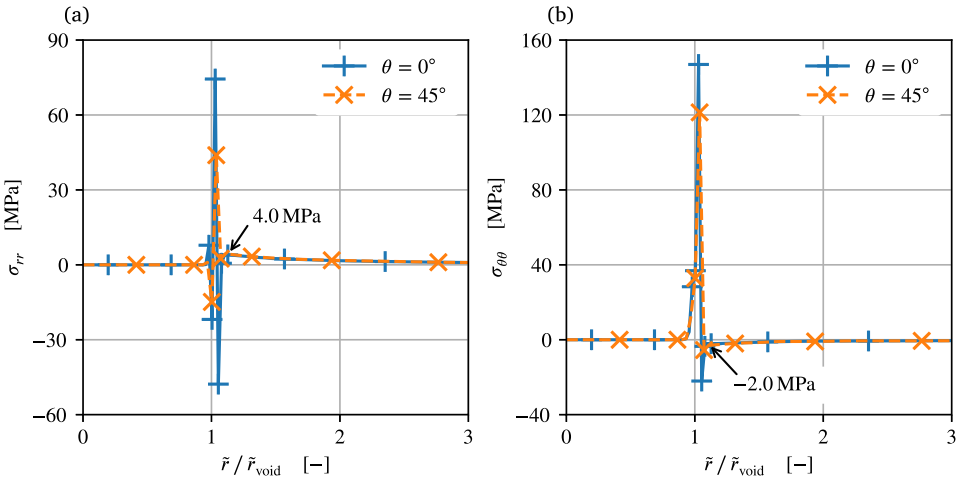

Fig. 5. Radial stress (a) and hoop stress (b) near a void in material without supersaturation as obtained from the equilibrium profile approach.

the void surface only reach about 4 MPa and −2 MPa, respectively, which is even more than an order of magnitude smaller than with the interpolation approach.

5.2. Stress-field around a void in a supersaturated bulk material

After establishing a better compliance with the expectations in the case without supersaturation, we investigate how the eigenstrain models affect the stress profile for a void in a material supersaturated with vacancies, for which we derived the analytical solution of stress in a sharp interface formulation. The derivation of the analytical solution is provided in Appendix A. We note that the analytical solution complies with the expected stress-free material in the non-supersaturated case ($S^{\mathrm{v}} = 1$). The supersaturation in the subsequent example was chosen to be $S^{\mathrm{v}} = 50$. Since the void will grow as a consequence of the supersaturation, we regard the stresses taken from the initial time step in order to focus on the stress predictions, only. At a later time the different kinetics of the two models produce different phase-field distributions and interface positions which would make a comparison more involved. For both approaches the void was initialized with a tanh-profile for the order parameter η, while we employed the $c^{\mathrm{v}}_{\mathrm{eq}}(\eta)$-relationship for initializing the vacancy concentration.

Plots of the radial and hoop stress for the interpolation approach in the directions along $\theta = 0°$ and $\theta = 45°$ are provided in Fig. 6 together with the analytically obtained stresses. Like in the case without supersaturation, the results show peaks within the interface, leading to a large deviation from the analytical solution. The radial and hoop stresses also deviate discernibly from the analytical solution in the bulk near the void surface.

The stresses obtained for the equilibrium profile approach for the void in a supersaturated matrix are shown in Fig. 7. Minor stress peaks also occur in this model within the interface but these are much smaller than those of the interpolation approach. In the bulk, the results from the equilibrium profile approach are very similar to the analytical solution even in the vicinity of the void surface.

In the supersaturated case we additionally performed a mesh-dependence study, to see if the stress fluctuations are merely the result of coarse mesh resolution. The stresses observed with a seven times higher mesh resolution than used above are displayed in Fig. 8 (a) for the interpolation approach and in Fig. 8 (b) for the equilibrium profile approach, each time evaluated in horizontal direction, $\theta = 0°$. In either case we additionally plot the eigenstrain profile and the analytical solution of the stresses. Note that the irregularities in the numerically obtained stress profiles stem from the very inhomogeneous mesh and we deem them to be of no physical significance. For the interpolation approach we find that the radial stress fluctuations can be reduced when using a finer mesh, but the overshoot of the hoop stress appears to be intrinsic to the interpolation approach, Eq. (2.7); the diagram suggests that this is due to the maximum eigenstrain occurring in the middle of the interface independent of mesh resolution. Both stress components also still show discernible deviations from the analytical solution in the bulk. In the case of the equilibrium profile

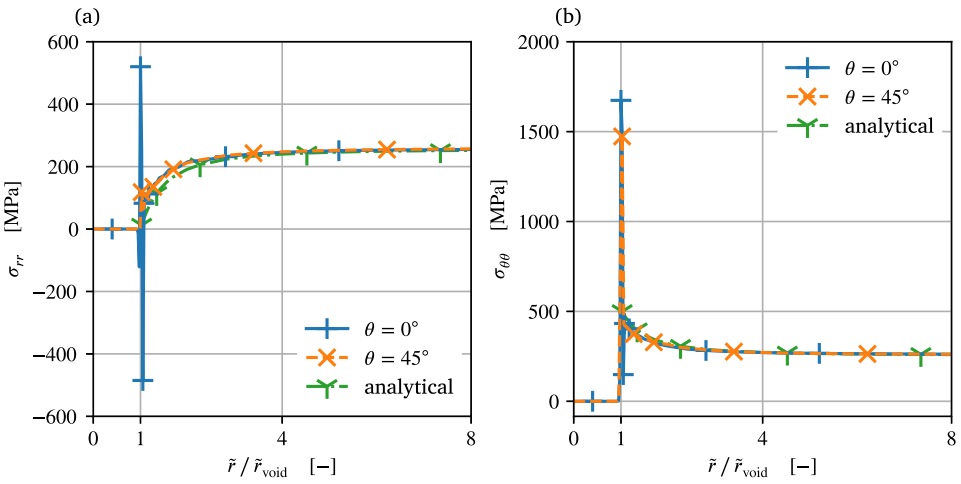

Fig. 6. Radial stress (a) and hoop stress (b) near a void in material with supersaturation $S^{\text{v}} = 50$ as obtained from the interpolation approach.

approach, Fig. 8 (b), the fluctuations of radial and hoop stresses are simultaneously reduced with a higher mesh resolution; this seems likewise expectable from the η-dependent eigenstrain which smoothly transitions from void to bulk. Moreover, the stress components match the analytical solution well up to the surface.

5.3. Elasto-diffusional growth of a void in a supersaturated bulk material under deformation

After validating the stress-coupling with the equilibrium profile approach in the two former subsections, we now demonstrate the influence of the elasto-diffusional coupling by regarding the growth of a void in a stressed material. Besides the undirected diffusion of vacancies, which will transport vacancies along concentration gradients, we expect in inhomogeneous stress states a drift of vacancies along gradients of what has been termed the elastic chemical potential [15,16,47]:

$$\mu^{\text{el}} := \frac{\delta \psi^{\text{el}}}{\delta c^{\text{v}}} = -\boldsymbol{\varepsilon}^{\text{v}} : \boldsymbol{\sigma} = -\frac{\varepsilon^{\text{v}}}{2} \frac{\text{tr}(\boldsymbol{\sigma})}{1+\nu}, \tag{5.1}$$

where we inserted Eq. (3.3) to obtain the last equality. The elastic chemical potential is in this case proportional to the trace of the (non-planar) stress tensor $\text{tr}(\boldsymbol{\sigma}) = \sigma_{11}+\sigma_{22}+\sigma_{33}$, where due to the plane-strain assumption we have $\sigma_{33} = \nu\left(\sigma_{11}+\sigma_{22}\right)$ with Poisson's ratio $\nu = (3K - 2G)/[2(3K + G)]$. Vacancies preferentially stay in (and drift towards) areas with small elastic chemical potential, which means in the current case, since $\varepsilon^{\text{v}} = -0.2$ is negative, that vacancies prefer regions with a hydrostatic compressive stress (negative trace) over areas with a hydrostatic tensile stress (positive trace).

As example for the elasto-diffusional coupling we choose a tensile deformation in $\tilde{x}$-, i.e. horizontal, direction, compare Fig. 9. A void is placed in a highly supersaturated material, $S^{\text{v}} = 1000$, and a dimensionless horizontal displacement $\tilde{u} = 4$ is applied instantly. The simulation is run until dimensionless time $\tilde{t} = 500$. Obviously, the resulting initial vacancy concentration of more than 0.1 and stresses on the order of up to 10 GPa are meaningless for any real material. The high values of supersaturation and strain are only chosen in order to detect the appearing coupled effects and the resulting growth clearly within a reasonable simulation time. However, similar effects are expected to appear also under less extreme conditions after much longer times.

In Fig. 10, the void growth indicated by the change of the dimensionless void radius $\Delta\tilde{r}_{\text{void}}$ for the tensile and transverse direction, $\theta = 0°$ and $\theta = 90°$, respectively, is displayed. Initially, the radius of the void surface, indicated by $\eta = 0.5$, grows faster along the transverse direction, as can be seen in Fig. 10 (a). However, in the long run, the void grows faster in the tensile direction, as may be read from Fig. 10 (b). In Fig. 11 (b), the initial ($\tilde{t} = 0$) and final distribution ($\tilde{t} = 500$) are opposed, clearly showing the anisotropic void growth. Notably, the void shape as a result of the coupled simulation does not show a simple, e.g. ellipsoidal shape.

The observations in this example may be rationalized in conjunction with the trace of the stress resulting only from the tensile load in the initial configuration, as displayed in Fig. 11 (a). Starting with a high supersaturation, we expect the void surface to act as vacancy sink, where the sink strength is slightly modified by the stress field from the tensile load, since the gradient of the elastic chemical potential across the surface is higher where the trace of the stress tensors is higher. Initially, we therefore expect the void to grow slightly faster along the transverse direction than along the tensile direction. This initial behavior may be regarded as dominated by surface reactions. However, while the concentration diminishes quicker on the surface in transverse direction, the higher elastic chemical potential around the transverse direction slows down further vacancy diffusion along the developing concentration gradient, since the gradient of the elastic chemical potential induces a drift in the opposite direction. By contrast, the diffusion is enhanced by the elasto-chemical drift around the tensile direction. Therefore, the void soon starts growing faster along the tensile direction than along the transverse direction in the diffusion dominated regime. We note that on the phenomenological level, such a developing anisotropy under stress is reminiscent of the so-called rafting of γ'-particles in Ni-based super-alloys, cf. for instance [48].

6. Discussion

The results presented in the last section clearly show that with the equilibrium profile approach the stress artifacts, which occur in and close to the diffuse interface in the more traditional interpolation approach, can be reduced considerably. The very high stress fluctuations displayed by the interpolation approach in the non-supersaturated case were found to be relatively less severe for a high supersaturation. But in conjunction with the deviations in the bulk, these fluctuations may still be expected to affect results of elastically coupled simulations of vacancy diffusion close to free surfaces. In the non-supersaturated and the highly supersaturated case, the equilibrium profile approach showed far lower deviations from the analytical solution both in the surface and in the adjacent bulk. For very high mesh resolutions, only the equilibrium profile approach showed no discernible stress fluctuations and clearly approached the analytical solution. Finally, we showed that the coupled elasto-diffusion with the equilibrium profile approach predicts anisotropic void growth in uniaxial tension. In the latter simulation we used very high supersaturations leading to unreasonably high stresses in order to speed-up the evolution. However, one

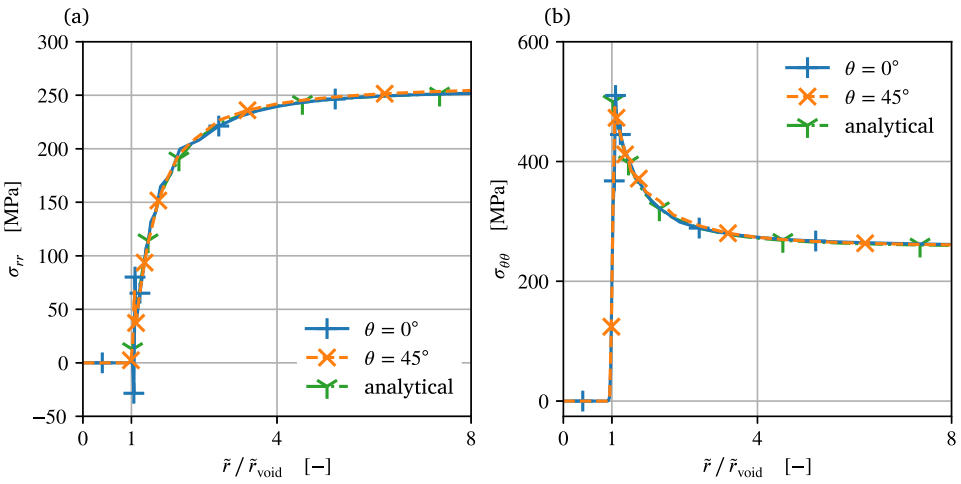

Fig. 7. Radial stress (a) and hoop stress (b) near a void in material with supersaturation $S^{\text{v}} = 50$ as obtained from the equilibrium profile approach.

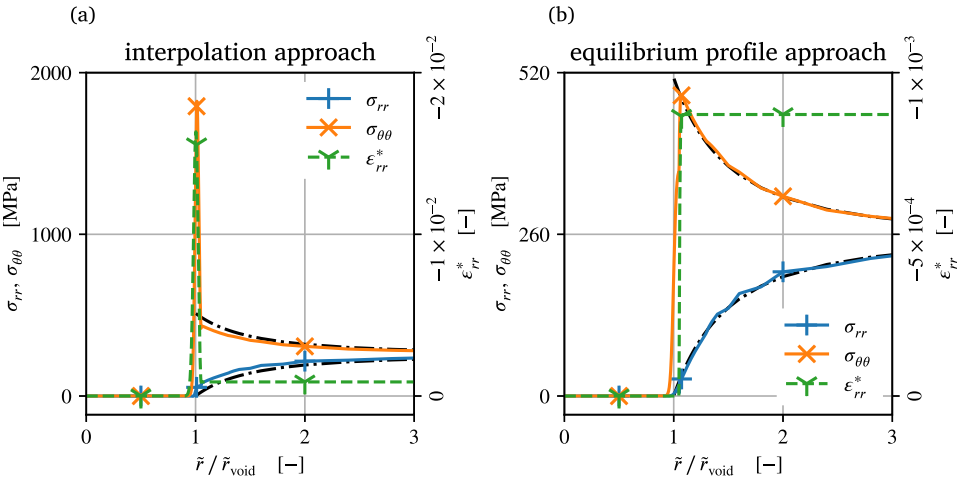

Fig. 8. Stress and eigenstrain components for a void under supersaturation simulated on a refined mesh as obtained from (a) the interpolation approach and (b) the equilibrium profile approach. For comparison, the analytical solutions for the stress components are displayed as black dash-dotted line.

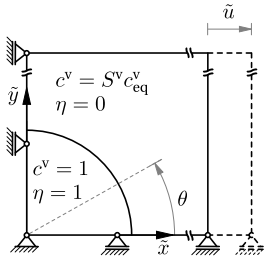

Fig. 9. Schematic of single void in supersaturated material with initial and boundary conditions including horizontal deformation.

may expect to observe similar effects with less extreme supersaturation and stress over longer times.

While the equilibrium profile approach rather emerged of necessity, a further analysis of the obtained equilibrium profile may justify the approach retroactively. When the obtained profile $c^{\text{v}}_{\text{eq}}(\eta)$ as given in Eq. (4.2) is plotted into a contour diagram of the dimensionless homogeneous energy $\tilde{\psi}^{\text{hom}}$, one finds that the curve is not far from a minimum energy path connecting the two phase minima, as may be obtained, e.g. from the nudged elastic band (NEB) method, see Fig. 12. The NEB method is frequently used in molecular statics to obtain transition pathways and energy barrier heights to be used in Monte Carlo simulations or transition state theory. The minimum energy pathway (MEP) obtained by the NEB method on the one hand passes the saddle point between two energy minima and on the other hand the path itself minimizes the energy in the sense that points on the path locally minimize the energy in a (hyper-)plane perpendicular to the path. The path is consequently perpendicular to the energy levels and thus parallel to the gradient of the energy, i.e. it is a so-called steepest descent path.[1] In transition state theory this path is considered to be the most likely 'reaction' path to be followed, when a system switches between two energy minimizing states. In the current example, the result of the NEB as displayed in Fig. 12 is the MEP between the bulk and void phase when only the dimensionless homogeneous energy density $\tilde{\psi}^{\text{hom}}$ is considered. Obviously, the equilibrium profile $c^{\text{v}}_{\text{eq}}(\eta)$ obtained from the relaxed flat surface is *not* the MEP for the homogeneous energy, cf. Fig. 12. But a deviation from this MEP is expected, since the equilibrium profile is obtained from minimizing the total energy, which also contains the surface contribution ψ^{gr} involving the gradients of the fields. Assuming that $c^{\text{v}}_{\text{eq}}(\eta)$ *is* the MEP[2] of the total energy, the equilibrium

[1] Indeed, the NEB is only designed to converge to an extremal steepest decent path, that is, the resulting path might also contain a ridge of maximal energy [49]. However, for the current energy the NEB obviously converged to an MEP.

[2] Actually, $c^{\text{v}}_{\text{eq}}(\eta)$ is assumed to be the projection of the MEP in the higher dimensional space involving the gradients of the fields to the c^{v}–η-plane.

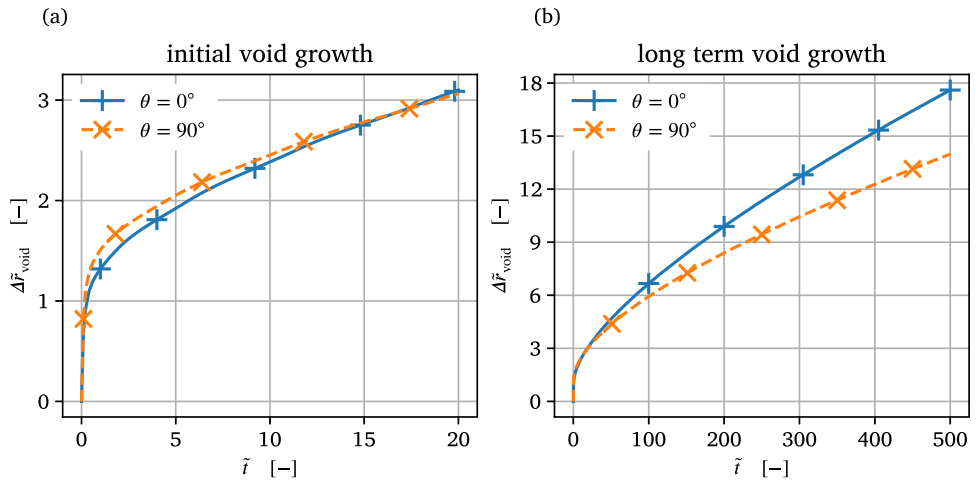

Fig. 10. Void growth (void-surface displacement from initial position) along tensile ($\theta = 0°$) and transverse ($\theta = 90°$) direction for a void under supersaturation and tensile deformation: (a) initial void growth up to dimensionless time 20, (b) void growth over the full simulation time.

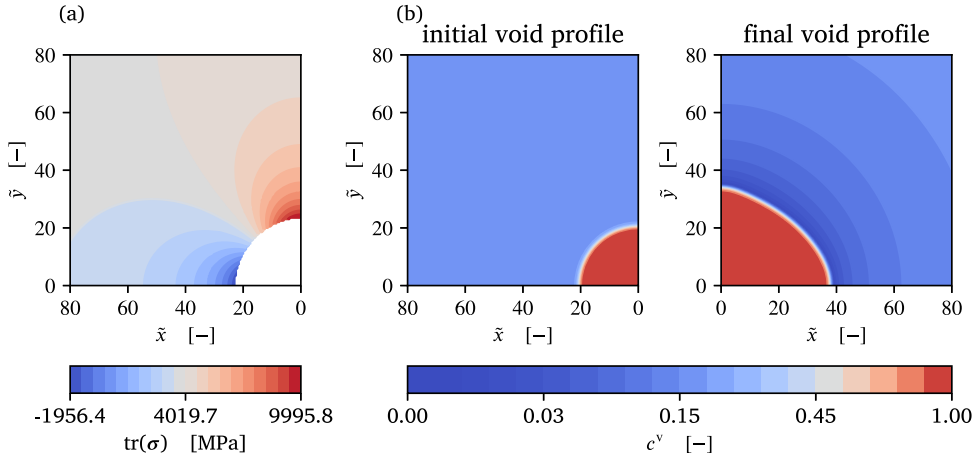

Fig. 11. Anisotropic growth of void when exposed to tensile load: (a) Contour plot of trace of stress $\mathrm{tr}(\boldsymbol{\sigma})$ resulting from tensile load in the initial state, (b) Contour plot of vacancy concentration in initial state ($\tilde{t} = 0$) and final state ($\tilde{t} = 500$).

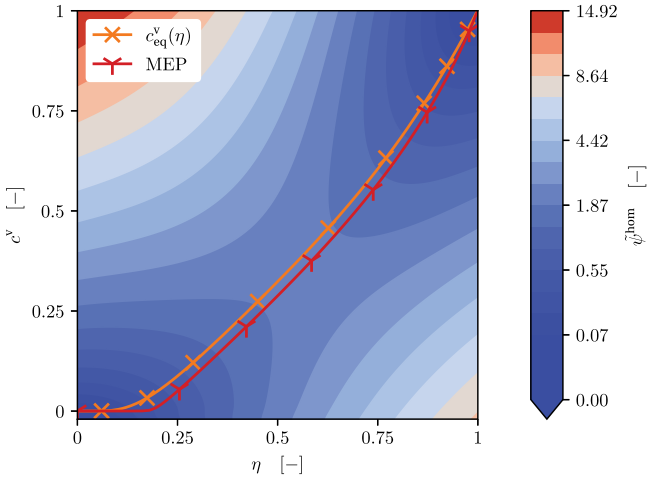

Fig. 12. Contour plot of dimensionless homogeneous free energy density with paths between bulk and void phase.

profile approach may be viewed as defining the elastic energy such that this path, which defines the coupled profiles of the order parameters across the surface, is also an MEP of the elastically coupled energy, since the elastic contribution vanishes along this path. Consequently, a flat surface in the elastically coupled calculation is supposed to likewise attain the profiles which comply with this MEP and in turn result in a stress-free surface. While the resulting stresses have been discussed in detail in Section 5, we now take a look at the energy density across the surface. We again oppose the equilibrium profile approach and the interpolation approach. In Fig. 13, the deviations in various energy density contributions $\Delta\tilde{\psi}^{\mathrm{contr}} = \tilde{\psi}^{\mathrm{approach,\,contr}} - \tilde{\psi}^{\mathrm{uncoupled,\,contr}}$ of the two coupled models from the model without elastic coupling are plotted as function of the order parameter η. The regarded contributions are the deviations in the homogeneous energy density $\Delta\tilde{\psi}^{\mathrm{hom}}$, the gradient energy density $\Delta\tilde{\psi}^{\mathrm{gr}}$, and the elastic energy density $\Delta\tilde{\psi}^{\mathrm{el}}$. Note that the elastic energy density of the uncoupled case vanishes, such that the latter 'deviation' is just the elastic energy of the coupled model, $\Delta\tilde{\psi}^{\mathrm{el}} = \tilde{\psi}^{\mathrm{el,\,approach}}$. The displayed results are deduced from numerically equilibrated flat-surface-profiles of c^{v} and η. For the equilibrations with regard to the uncoupled and the two coupled energies, the phase fields were each time initialized with a tanh-profile for η and the concentration profile obtained from the former through Eq. (4.1). The equilibrated profiles were obtained with a mesh similar to the one shown in Fig. 1, but with three more levels of refinement in the center.

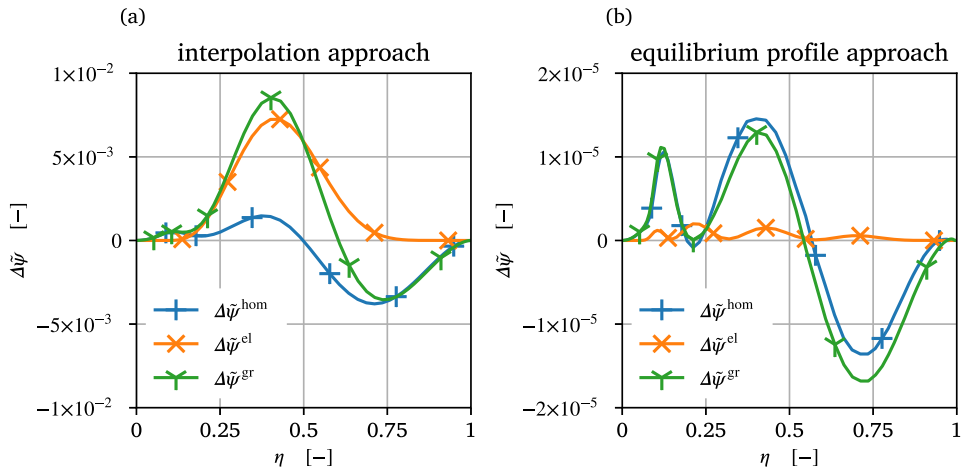

Fig. 13. Energy deviations from the uncoupled system (where $\tilde{\psi}^{\mathrm{el}} \equiv 0$) for (a) interpolation approach and (b) equilibrium profile approach.

The deviations in the different energy density contributions are displayed in Fig. 13 as a function of the order parameter η, which is used to parameterize the position within the flat surface invariant of the employed approach. The absolute energetic differences are small for both coupled approaches, where we note that different vertical scales are used for the deviations in case of the interpolation approach, Fig. 13 (a), and of the equilibrium profile approach, Fig. 13 (b). In case of the interpolation approach the deviations are roughly on the order of 10^{-2} for the gradient and the elastic energy densities and on the order of 10^{-3} in case of the homogeneous energy density. In case of the equilibrium profile approach, the deviations are roughly on the order of 10^{-5} for the gradient and the homogeneous energy densities and on the order of 10^{-6} in case of the elastic energy density. In comparison, the energy deviations from the uncoupled system is three orders of magnitude larger for the interpolation approach than for the equilibrium profile approach. Notably, the (deviation of the) elastic energy density is nearly four orders of magnitude larger for the interpolation approach. From the very low deviations in the energy density contributions observed for the equilibrium profile approach we see that the phase-field profiles across a flat interface remain virtually unchanged upon the elastic coupling.

During the review we were made aware of the work by Aagesen and co-workers [50], who used a somewhat similar equilibrium concentration depending on a non-conserved order parameter in a phase-field formulation for multiphase materials in the spirit of Kim, Kim and Suzuki [51] based on a grand potential formulation [52]. In contrast to the current approach, the equilibrium concentration profile in [50] is obtained from an interpolation rather than from an equilibrated system. But with this proceeding, Aagesen and co-workers achieved a decoupling of bulk energy and interfacial energy contributions. In a similar way, the current equilibrium profile approach may be viewed as decoupling the energies of bulk and surface stresses, where the latter are deemed negligible in the current work. It appears promising to address the relation between the two approaches in more detail.

7. Conclusion

The phase-field method offers an important perspective for modeling the concurrent evolution of defects and defect concentrations in crystals in a spatially resolved fashion. Defect interactions usually involve eigenstress fields induced by the defects and a coupling of phase-field descriptions with elastic effects is needed to capture these interactions. We think that the current work provides convincing evidence and theoretical justification for pursuing the equilibrium profile approach in phase-field models of elasto-diffusion of vacancies. It appears that this approach could also be easily extended to phase-field models which additional account for interstitial concentrations, though the coupling of the equilibrium profiles of different point defects species across the surface may require some further investigations. The approach should also be transferable to electrically charged point defects in phase-field models, since electrical charges are usually likewise modeled proportional to the point defect concentration, which would lead to charge accumulations in surfaces when variants of the interpolation approach would be employed.

The equilibrium profile approach does of course also entail certain limitations which require further investigations. It is for example known that the equilibrium vacancy concentration at a surface depends on the curvature of the surface. In the regarded cases this curvature dependence seemed negligible, but this may be different for very small voids (high curvature) or also at lower temperatures, when the equilibrium concentration is much lower to begin with and the relative influence of surface curvature may be larger. The latter point leads over to the fact that the equilibrium vacancy concentration is of course temperature dependent and that, accordingly, the equilibrium profile will in general likewise have to be a function of temperature, $c^{\mathrm{v}}_{\mathrm{eq}}(\eta, T)$. The equilibrium profile will in fact also depend on all other parameters in the energy density, most notably on the gradient coefficients κ^{c} and κ^{η}. How to deal with dependencies of the equilibrium profile upon field quantities like temperature and surface curvature shall be topic of future research.

CRediT authorship contribution statement

Kevin A. Pendl: Methodology, Software, Visualization, Writing – original draft, Writing – review & editing. **Thomas Hochrainer:** Conceptualization, Methodology, Writing – original draft, Writing – review & editing.

Declaration of competing interest

The authors declare that they have no known competing financial interests or personal relationships that could have appeared to influence the work reported in this paper.

Data availability

Data will be made available on request.

Acknowledgements

The authors thank Srujan Rokkam for helpful discussions and providing a source-code of his phase-field model.

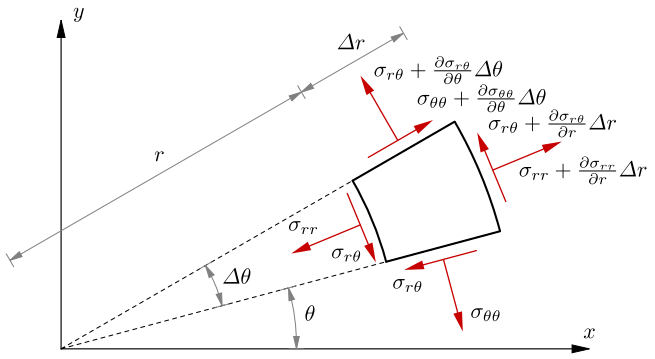

Fig. 14. Infinitesimal area element with stresses in polar coordinates.

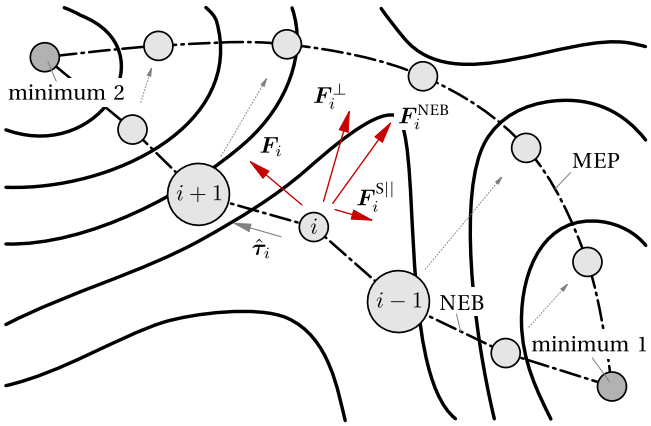

Fig. 15. Schematic depiction of the nudged elastic band method (based on [53]). The solid lines indicate iso-(hyper-)surfaces of an energy potential V.

Appendix A

In this Appendix we derive the analytical solution for plane axisymmetric problems with volumetric misfit in polar coordinates. Starting with the sum of the forces in radial and tangent direction on an infinitesimal area element, cf. Fig. 14, one arrives at the equilibrium equations in polar coordinates,

$$\frac{\partial \sigma_{rr}}{\partial r} + \frac{1}{r}\frac{\partial \sigma_{r\theta}}{\partial \theta} + \frac{1}{r}\left(\sigma_{rr} - \sigma_{\theta\theta}\right) = 0, \tag{A.1a}$$

$$\frac{\partial \sigma_{r\theta}}{\partial r} + \frac{1}{r}\frac{\partial \sigma_{\theta\theta}}{\partial \theta} + \frac{2\sigma_{r\theta}}{r} = 0. \tag{A.1b}$$

Considering the axisymmetry of the underlying problem, i.e. $\sigma_{r\theta} = 0$ and $\frac{\partial(\cdot)}{\partial\theta} = 0$, the equilibrium equations reduce to the single equation

$$\frac{\partial \sigma_{rr}}{\partial r} + \frac{1}{r}\left(\sigma_{rr} - \sigma_{\theta\theta}\right) = 0. \tag{A.2}$$

If only radial displacements are considered, i.e. $u_r := u, u_\theta = 0$, the elementary strain–displacement relations read

$$\varepsilon_{rr} = \frac{\partial u}{\partial r}, \qquad \varepsilon_{\theta\theta} = \frac{u}{r}, \qquad \varepsilon_{r\theta} = 0\,. \tag{A.3}$$

The appearing lattice misfit is incorporated in the form of (Eq. (2.7) and (2.8))

$$\varepsilon^*_{rr} = \varepsilon^*_{\theta\theta} = \frac{\varepsilon^{\mathrm{v}}}{2}\left(c^{\mathrm{v}} - c^{\mathrm{v}}_{\mathrm{eq}}\right) = \frac{\varepsilon^{\mathrm{v}}}{2}\left(S^{\mathrm{v}} - 1\right)c^{\mathrm{v}}_{\mathrm{eq}}, \qquad \varepsilon^*_{r\theta} = 0\,. \tag{A.4}$$

We point out that in the considered examples we always assume a spatially homogeneous vacancy concentration c^{v}, such that also the eigenstrain components are constants. We accordingly introduce the constant $\varepsilon^* = \varepsilon^*_{rr} = \varepsilon^*_{\theta\theta}$. In order to combine Eqs. (A.2) and (A.3) we employ Hooke's law in its stress-based form for plane-strain and the relation between total strain, elastic strain and eigenstrain, i.e. $\boldsymbol{\varepsilon}^{\mathrm{el}} = \boldsymbol{\varepsilon} - \boldsymbol{\varepsilon}^*$. Consequently we obtain

$$\sigma_{rr} = \frac{E}{(1+\nu)(1-2\nu)}\left[\nu(\varepsilon_{\theta\theta} - \varepsilon^*) + (1-\nu)(\varepsilon_{rr} - \varepsilon^*)\right], \tag{A.5a}$$

$$\sigma_{\theta\theta} = \frac{E}{(1+\nu)(1-2\nu)}\left[\nu(\varepsilon_{rr} - \varepsilon^*) + (1-\nu)(\varepsilon_{\theta\theta} - \varepsilon^*)\right], \tag{A.5b}$$

where E is Young's modulus and ν Poisson's ratio. If Eqs. (A.3), (A.5a) and (A.5b) are inserted in (A.2) one arrives at

$$(1-\nu)\left[\frac{\partial^2 u}{\partial r^2} + \frac{1}{r}\frac{\partial u}{\partial r} - \frac{u}{r^2}\right] = 0\,. \tag{A.6}$$

The term inside the bracket is an ordinary differential equation the solutions of which are of the form

$$u = C_1 r + \frac{C_2}{r}\,, \tag{A.7}$$

with C_1 and C_2 being constants obtained from boundary conditions. If Eq. (A.7) is inserted into Eqs. (A.5a) and (A.5b), while considering the strain–displacement relations of Eq. (A.3), one obtains for the stresses

$$\sigma_{rr} = \frac{E}{(1+\nu)(1-2\nu)}\left[C_1 - C_2(1-2\nu)\frac{1}{r^2} - \varepsilon^*\right], \tag{A.8a}$$

$$\sigma_{\theta\theta} = \frac{E}{(1+\nu)(1-2\nu)}\left[C_1 + C_2(1-2\nu)\frac{1}{r^2} - \varepsilon^*\right]. \tag{A.8b}$$

The constants C_1 and C_2 are obtained from boundary conditions. At the free surface of the void we have $\sigma_{rr}(r = r_{\mathrm{void}}) = 0$ and we impose that the radial displacement vanishes at the outer boundary, i.e. $u(r = r_{\mathrm{far}}) = 0$, with r_{far} being the distance between the origin of the void and the boundary of the considered circular domain. These boundary conditions yield the constants

$$C_1 = \frac{\varepsilon^*}{1 + (1-2\nu)\dfrac{r^2_{\mathrm{far}}}{r^2_{\mathrm{void}}}}, \qquad C_2 = -C_1\, r^2_{\mathrm{far}}\,. \tag{A.9}$$

Since we actually do not consider a circular but a quadratic domain in Section 5.2, this analytical solution is not obviously applicable. However, for symmetry reasons, the employed conditions, $\sigma_{r\theta} = 0$, $\frac{\partial(\cdot)}{\partial\theta} = 0$, and $u_\theta = 0$ as well as vanishing radial displacements on the outer boundary are fulfilled along the horizontal direction, $\theta = 0°$, and along the diagonal direction, $\theta = 45°$. The solutions in these directions are different because r_{far} denotes in this case the distance from the void center to the point on the outer surface, such that $\tilde{r}_{\mathrm{far}} = 200$ in horizontal and $\tilde{r}_{\mathrm{far}} = \sqrt{2}\,200$ in diagonal direction, each time in dimensionless length units. However, the domain is large enough to make the difference between the two solutions so small, that it would be hardly discernible in the plots in Section 5.2. In these plots, the displayed analytical solution is always the one for $\theta = 0°$.

Appendix B

In this appendix we give a brief description of the nudged elastic band (NEB) method [54], which is commonly employed to obtain so-called minimum energy paths (MEP) between two (local) energy minima. A path in configuration space is called an MEP if every point on the path is at an energy minimum in all directions perpendicular to the path, which means that the path is perpendicular to the iso-(hyper-)surfaces of the energy potential V, compare Fig. 15. An MEP is consequently a so-called steepest descent path and it passes through (at least) one saddle point, which represents the maximum energy along this path [53], while it also marks the minimal energy barrier which needs to be overcome when changing from one minimum to the other. Each image i represents a *configuration of the system* along the path. In the nudged elastic band method the points are modeled as being connected by springs. Each image is then subject to a force (cf. Fig. 15),

$$\boldsymbol{F}_i^{\mathrm{NEB}} = \boldsymbol{F}_i^{\mathrm{S}||} + \boldsymbol{F}_i^{\perp}, \tag{B.1}$$

where $\boldsymbol{F}_i^{S||}$ are spring forces that act parallel to the path while $\boldsymbol{F}_i^{\perp}$ are the forces due to the energy potential that act perpendicular to the path. The spring forces ensure equal spacing of the images along the path and are calculated as

$$\boldsymbol{F}_i^{S||} = k\left(\|\boldsymbol{R}_{i+1} - \boldsymbol{R}_i\| - \|\boldsymbol{R}_i - \boldsymbol{R}_{i-1}\|\right)\hat{\boldsymbol{\tau}}_i, \tag{B.2}$$

with k being a spring constant, $\boldsymbol{R}_i$ is the position in state space of image i and $\hat{\boldsymbol{\tau}}_i$ is a suitably defined local unit tangent to the path at image i. The force perpendicular to the path is given by,

$$\boldsymbol{F}_i^{\perp} = \boldsymbol{F}_i - \left(\boldsymbol{F}_i \cdot \hat{\boldsymbol{\tau}}_i\right)\hat{\boldsymbol{\tau}}_i, \tag{B.3}$$

with $\boldsymbol{F}_i = -\boldsymbol{\nabla} V(\boldsymbol{R}_i)$ being the negative gradient of the energy potential $V(\boldsymbol{R})$ at image i. We adopted the tangent estimate from [55], which is based on the non-normalized tangent vector defined in dependence on the energy potential as

$$\boldsymbol{\tau}_i = \begin{cases} \boldsymbol{\tau}_i^{+}\Delta V_i^{\max} + \boldsymbol{\tau}_i^{-}\Delta V_i^{\min} & \text{if } V_{i+1} > V_{i-1} \\ \boldsymbol{\tau}_i^{+}\Delta V_i^{\min} + \boldsymbol{\tau}_i^{-}\Delta V_i^{\max} & \text{if } V_{i+1} < V_{i-1} \end{cases}, \tag{B.4}$$

where $\boldsymbol{\tau}_i^{+} = \boldsymbol{R}_{i+1} - \boldsymbol{R}_i$, $\boldsymbol{\tau}_i^{-} = \boldsymbol{R}_i - \boldsymbol{R}_{i-1}$, $\Delta V_i^{\max} = \max(|V_{i+1} - V_i|, |V_{i-1} - V_i|)$, and $\Delta V_i^{\min} = \min(|V_{i+1} - V_i|, |V_{i-1} - V_i|)$. The normalized tangent is then obtained as $\hat{\boldsymbol{\tau}}_i = \boldsymbol{\tau}_i / |\boldsymbol{\tau}_i|$.

An NEB calculation starts from an initial (often linear) pathway and the image positions are iteratively shifted in the force direction,

$$\boldsymbol{R}_i \mapsto \boldsymbol{R}_i + \alpha \boldsymbol{F}_i^{\mathrm{NEB}}, \tag{B.5}$$

with a parameter α. The process is stopped when the remaining forces are sufficiently small in a suitable norm. This results in an (approximate) steepest descent path with equally spaced images, because $\boldsymbol{F}_i^{\perp}$ and $\boldsymbol{F}_i^{S||}$ need to be small simultaneously.

In the current work we obtained the MEP in Fig. 12 numerically by adopting and modifying the 'Minimum Energy Path Tools' Python package `mep` [43,56], which is a package that contains various methods for finding the minimal energy path (originally in molecular statics) based on the publications by Henkelman et al. [55,57]. The provided energy in the package was substituted with the homogeneous energy Eq. (2.3) and the path was discretized with 101 images. We used the spring constant $k = 1$ and the parameter $\alpha = 4 \times 10^{-3}$. The stop criterion was set to $F^{\mathrm{NEB}} < 5 \times 10^{-3}$, where F^{NEB} is the norm of the global force vector,

$$F^{\mathrm{NEB}} = \sqrt{\sum_i \|\boldsymbol{F}_i^{\mathrm{NEB}}\|^2}, \tag{B.6}$$

where the sum runs through the images along the path except for the fixed end-points in the known minima.

References

[1] G.S. Was, Fundamentals of Radiation Materials Science: Metals and Alloys, second ed., Springer, New York, ISBN: 978-1-4939-3436-2, 2017.

[2] M. Zehetbauer, V. Seumer, Cold work hardening in stages IV and V of F.C.C. metals—I. Experiments and interpretation, Acta Metall. Mater. (ISSN: 09567151) 41 (2) (1993) 577–588, http://dx.doi.org/10.1016/0956-7151(93)90088-A.

[3] T. Ungár, E. Schafler, P. Hanák, S. Bernstorff, M. Zehetbauer, Vacancy production during plastic deformation in copper determined by in situ X-ray diffraction, Mater. Sci. Eng. A (ISSN: 09215093) 462 (1–2) (2007) 398–401, http://dx.doi.org/10.1016/j.msea.2006.03.156.

[4] A.D. Brailsford, R. Bullough, The rate theory of swelling due to void growth in irradiated metals, J. Nucl. Mater. (ISSN: 00223115) 44 (2) (1972) 121–135, http://dx.doi.org/10.1016/0022-3115(72)90091-8.

[5] H. Wiedersich, On the theory of void formation during irradiation, Radiat. Eff. (ISSN: 0033-7579) 12 (1–2) (1972) 111–125, http://dx.doi.org/10.1080/00337577208231128.

[6] P. Noell, J. Carroll, K. Hattar, B. Clark, B. Boyce, Do voids nucleate at grain boundaries during ductile rupture? Acta Mater. (ISSN: 1359-6454) 137 (2017) 103–114, http://dx.doi.org/10.1016/j.actamat.2017.07.004.

[7] P.J. Noell, J.E.C. Sabisch, D.L. Medlin, B.L. Boyce, Nanoscale conditions for ductile void nucleation in copper: Vacancy condensation and the growth-limited microstructural state, Acta Mater. (ISSN: 13596454) 184 (2020) 211–224, http://dx.doi.org/10.1016/j.actamat.2019.11.022.

[8] L.-Q. Chen, Phase-field models for microstructure evolution, Annu. Rev. Mater. Res. 32 (1) (2002) 113–140, http://dx.doi.org/10.1146/annurev.matsci.32.112001.132041, (ISSN: 1531-7331, 1545-4118).

[9] N. Moelans, B. Blanpain, P. Wollants, An introduction to phase-field modeling of microstructure evolution, CALPHAD (ISSN: 03645916) 32 (2) (2008) 268–294, http://dx.doi.org/10.1016/j.calphad.2007.11.003.

[10] D.O. Kharchenko, V.O. Kharchenko, Y.M. Ovcharenko, O.B. Lysenko, I.A. Shuda, L. Wu, R. Pan, Phase field modelling voids nucleation and growth in binary systems, Condens. Matter Phys. 21 (1) (2018) 13002, http://dx.doi.org/10.5488/CMP.21.13002, (ISSN: 1607324X, 22249079).

[11] Z. Xiao, Y. Wang, S. Hu, Y. Li, S.-Q. Shi, A quantitative phase-field model of gas bubble evolution in UO2, Comput. Mater. Sci. (ISSN: 09270256) 184 (2020) 109867, http://dx.doi.org/10.1016/j.commatsci.2020.109867.

[12] S. Hu, C.H. Henager, H.L. Heinisch, M. Stan, M.I. Baskes, S.M. Valone, Phase-field modeling of gas bubbles and thermal conductivity evolution in nuclear fuels, J. Nucl. Mater. (ISSN: 00223115) 392 (2) (2009) 292–300, http://dx.doi.org/10.1016/j.jnucmat.2009.03.017.

[13] M. Javanbakht, M.S. Ghaedi, Phase field approach for void dynamics with interface stresses at the nanoscale, Internat. J. Engrg. Sci. (ISSN: 00207225) 154 (2020) 103279, http://dx.doi.org/10.1016/j.ijengsci.2020.103279.

[14] M.S. Ghaedi, M. Javanbakht, Effect of a thermodynamically consistent interface stress on thermal-induced nanovoid evolution in NiAl, Math. Mech. Solids 26 (9) (2021) 1320–1336, http://dx.doi.org/10.1177/1081286520986603, (ISSN: 1081-2865, 1741-3028).

[15] H.-C. Yu, W. Lu, Dynamics of the self-assembly of nanovoids and nanobubbles in solids, Acta Mater. (ISSN: 13596454) 53 (6) (2005) 1799–1807, http://dx.doi.org/10.1016/j.actamat.2004.12.029.

[16] H.-C. Yu, W. Lu, Ordering of nanovoids in an anisotropic solid driven by surface misfit, J. Comput. Theor. Nanosci. 2 (2) (2005) 256–262, http://dx.doi.org/10.1166/jctn.2005.109, (ISSN: 15461955, 15461963).

[17] A.A. Semenov, C.H. Woo, Phase-field modeling of void formation and growth under irradiation, Acta Mater. (ISSN: 13596454) 60 (17) (2012) 6112–6119, http://dx.doi.org/10.1016/j.actamat.2012.07.049.

[18] S.Y. Hu, M.I. Baskes, M. Stan, Phase-field modeling of microvoid evolution under elastic-plastic deformation, Appl. Phys. Lett. 90 (8) (2007) 081921, http://dx.doi.org/10.1063/1.2709908, (ISSN: 0003-6951, 1077-3118).

[19] S. Rokkam, A. El-Azab, P. Millett, D. Wolf, Phase field modeling of void nucleation and growth in irradiated metals, Modelling Simul. Mater. Sci. Eng. 17 (6) (2009) 064002, http://dx.doi.org/10.1088/0965-0393/17/6/064002, (ISSN: 0965-0393, 1361-651X).

[20] Y.-Y. Wang, J.-H. Ding, W.-B. Liu, S.-S. Huang, X.-Q. Ke, Y.-Z. Wang, C. Zhang, J.-J. Zhao, Irradiation-induced void evolution in iron: A phase-field approach with atomistic derived parameters, Chin. Phys. B (ISSN: 1674-1056) 26 (2) (2017) 026102, http://dx.doi.org/10.1088/1674-1056/26/2/026102.

[21] P.C. Millett, S. Rokkam, A. El-Azab, M. Tonks, D. Wolf, Void nucleation and growth in irradiated polycrystalline metals: a phase-field model, Modelling Simul. Mater. Sci. Eng. 17 (6) (2009) 064003, http://dx.doi.org/10.1088/0965-0393/17/6/064003, (ISSN: 0965-0393, 1361-651X).

[22] S. Rokkam, A. El-Azab, A diffuse interface model for void formation under non-equilibrium irradiation, MRS Online Proc. Libr. 1363 (2011) 704, http://dx.doi.org/10.1557/opl.2011.1529, (ISSN: 0272-9172, 1946-4274).

[23] P.C. Millett, A. El-Azab, S. Rokkam, M. Tonks, D. Wolf, Phase-field simulation of irradiated metals, Comput. Mater. Sci. (ISSN: 09270256) 50 (3) (2011) 949–959, http://dx.doi.org/10.1016/j.commatsci.2010.10.034.

[24] T. Hochrainer, A. El-Azab, A sharp interface model for void growth in irradiated materials, Phil. Mag. 95 (9) (2015) 948–972, http://dx.doi.org/10.1080/14786435.2015.1009516, (ISSN: 1478-6435, 1478-6443).

[25] K. Ahmed, A. El-Azab, An analysis of two classes of phase field models for void growth and coarsening in irradiated crystalline solids, Mater. Theory (ISSN: 2509-8012) 2 (1) (2018) 1, http://dx.doi.org/10.1186/s41313-017-0008-y.

[26] D. Schneider, O. Tschukin, A. Choudhury, M. Selzer, T. Böhlke, B. Nestler, Phase-field elasticity model based on mechanical jump conditions, Comput. Mech. 55 (5) (2015) 887–901, http://dx.doi.org/10.1007/s00466-015-1141-6, (ISSN: 0178-7675, 1432-0924).

[27] A.G. Khachaturyan, Theory of Structural Transformations in Solids, Wiley, New York, ISBN: 978-0-471-07873-9, 1983.

[28] K. Ammar, B. Appolaire, G. Cailletaud, S. Forest, Combining phase field approach and homogenization methods for modelling phase transformation in elastoplastic media, Eur. J. Comput. Mech. 18 (5–6) (2009) 485–523, http://dx.doi.org/10.3166/ejcm.18.485-523, (ISSN: 1779-7179, 1958-5829).

[29] A. Durga, P. Wollants, N. Moelans, Evaluation of interfacial excess contributions in different phase-field models for elastically inhomogeneous systems, Modelling Simul. Mater. Sci. Eng. 21 (5) (2013) 055018, http://dx.doi.org/10.1088/0965-0393/21/5/055018, (ISSN: 0965-0393, 1361-651X).

[30] A. Villani, A multi-physics modelling framework to describe the behaviour of nano-scale multilayer systems undergoing irradiation damage (Ph.D. thesis), Ecole Nationale Superieure des Mines de Paris, Paris (France), 2015.

[31] M. Javanbakht, M.S. Ghaedi, Nanovoid induced multivariant martensitic growth under negative pressure: Effect of misfit strain and temperature on PT threshold stress and phase evolution, Mech. Mater. (ISSN: 01676636) 151 (2020) 103627, http://dx.doi.org/10.1016/j.mechmat.2020.103627.

[32] M. Javanbakht, M.S. Ghaedi, E. Barchiesi, A. Ciallella, The effect of a pre-existing nanovoid on martensite formation and interface propagation: a phase field study, Math. Mech. Solids 26 (1) (2021) 90–109, http://dx.doi.org/10.1177/1081286520948118, (ISSN: 1081-2865, 1741-3028).
[33] S. Rokkam, Phasefield Modeling of Void Nucleation and Growth in Irradiated Materials (Ph.D. thesis), The Florida State University, Ann Arbor, 2011.
[34] J.P. Hirth, J. Lothe, Theory of Dislocations, McGraw-Hill, New York, 1968.
[35] B.D. Coleman, W. Noll, The thermodynamics of elastic materials with heat conduction and viscosity, Arch. Ration. Mech. Anal. 13 (1) (1963) 167–178, http://dx.doi.org/10.1007/BF01262690, (ISSN: 0003-9527, 1432-0673).
[36] J.W. Cahn, On spinodal decomposition, Acta Metall. (ISSN: 00016160) 9 (9) (1961) 795–801, http://dx.doi.org/10.1016/0001-6160(61)90182-1.
[37] S.M. Allen, J.W. Cahn, A microscopic theory for antiphase boundary motion and its application to antiphase domain coarsening, Acta Metall. (ISSN: 00016160) 27 (6) (1979) 1085–1095, http://dx.doi.org/10.1016/0001-6160(79)90196-2.
[38] J.W. Cahn, J.E. Hilliard, Free energy of a nonuniform system. I. Interfacial free energy, J. Chem. Phys. 28 (2) (1958) 258–267, http://dx.doi.org/10.1063/1.1744102, (ISSN: 0021-9606, 1089-7690).
[39] A.A. Wheeler, W.J. Boettinger, G.B. McFadden, Phase-field model for isothermal phase transitions in binary alloys, Phys. Rev. A 45 (10) (1992) 7424–7439, http://dx.doi.org/10.1103/PhysRevA.45.7424, (ISSN: 1050-2947, 1094-1622).
[40] M.J. Caturla, N. Soneda, E. Alonso, B.D. Wirth, T. Díaz de la Rubia, J.M. Perlado, Comparative study of radiation damage accumulation in Cu and Fe, J. Nucl. Mater. (ISSN: 00223115) 276 (1–3) (2000) 13–21, http://dx.doi.org/10.1016/S0022-3115(99)00220-2.
[41] S. DeWitt, S. Rudraraju, D. Montiel, W.B. Andrews, K. Thornton, PRISMS-PF: A general framework for phase-field modeling with a matrix-free finite element method, Npj Comput. Mater. (ISSN: 2057-3960) 6 (1) (2020) 29, http://dx.doi.org/10.1038/s41524-020-0298-5.
[42] P. Virtanen, R. Gommers, T.E. Oliphant, M. Haberland, T. Reddy, D. Cournapeau, E. Burovski, P. Peterson, W. Weckesser, J. Bright, S.J. van der Walt, M. Brett, J. Wilson, K.J. Millman, N. Mayorov, A.R.J. Nelson, E. Jones, R. Kern, E. Larson, C.J. Carey, İ. Polat, Y. Feng, E.W. Moore, J. VanderPlas, D. Laxalde, J. Perktold, R. Cimrman, I. Henriksen, E.A. Quintero, C.R. Harris, A.M. Archibald, A.H. Ribeiro, F. Pedregosa, P. van Mulbregt, SciPy 1.0 Contributors, SciPy 1.0: fundamental algorithms for scientific computing in Python, Nature Methods 17 (3) (2020) 261–272, http://dx.doi.org/10.1038/s41592-019-0686-2, (ISSN: 1548-7091, 1548-7105).
[43] G. van Rossum, F.L. Drake, Python 3 Reference Manual, CreateSpace, Scotts Valley, CA, ISBN: 978-1-4414-1269-0, 2009.
[44] Y. Mishin, M.R. Sørensen, A.F. Voter, Calculation of point-defect entropy in metals, Phil. Mag. A 81 (11) (2001) 2591–2612, http://dx.doi.org/10.1080/01418610108216657, (ISSN: 0141-8610, 1460-6992).
[45] N.J. Simon, E.S. Drexler, R. Reed, Properties of Copper and Copper Alloys at Cryogenic Temperatures. Final Report, Technical Report PB-92-172766/XAB, NIST/MONO–177, 5340308, National Institute of Standards and Technology (MSEL), Boulder, CO (United States). Materials Reliability Div., 1992, pp. PB–92–172766/XAB, NIST/MONO–177, 5340308.
[46] L.B. Freund, S. Suresh, Thin Film Materials: Stress, Defect Formation and Surface Evolution, first ed., Cambridge University Press, 2004, http://dx.doi.org/10.1017/CBO9780511754715, ISBN: 978-0-521-82281-7 978-0-521-52977-8 978-0-511-75471-5.
[47] S.Y. Hu, L.Q. Chen, Solute segregation and coherent nucleation and growth near a dislocation—a phase-field model integrating defect and phase microstructures, Acta Mater. (ISSN: 13596454) 49 (3) (2001) 463–472, http://dx.doi.org/10.1016/S1359-6454(00)00331-1.
[48] D.Y. Li, L.Q. Chen, Computer simulation of morphological evolution and rafting of gammaprime particles in Ni-based superalloys under applied stresses, Scr. Mater. 37 (9) (1997) 1271–1277, http://dx.doi.org/10.1016/S1359-6462(97)00276-5.
[49] D. Sheppard, G. Henkelman, Paths to which the nudged elastic band converges, J. Comput. Chem. (ISSN: 01928651) 32 (8) (2011) 1769–1771, http://dx.doi.org/10.1002/jcc.21748.
[50] L.K. Aagesen, Y. Gao, D. Schwen, K. Ahmed, Grand-potential-based phase-field model for multiple phases, grains, and chemical components, Phys. Rev. E 98 (2018) 023309, http://dx.doi.org/10.1103/PhysRevE.98.023309.
[51] S.G. Kim, W.T. Kim, T. Suzuki, Phase-field model for binary alloys, Phys. Rev. E 60 (1999) 7186–7197, http://dx.doi.org/10.1103/PhysRevE.60.7186.
[52] M. Plapp, Unified derivation of phase-field models for alloy solidification from a grand-potential functional, Phys. Rev. E 84 (2011) 031601, http://dx.doi.org/10.1103/PhysRevE.84.031601.
[53] D. Sheppard, R. Terrell, G. Henkelman, Optimization methods for finding minimum energy paths, J. Chem. Phys. 128 (13) (2008) 134106, http://dx.doi.org/10.1063/1.2841941, (ISSN: 0021-9606, 1089-7690).
[54] H. Jónsson, G. Mills, K.W. Jacobsen, Nudged elastic band method for finding minimum energy paths of transitions, in: Classical and Quantum Dynamics in Condensed Phase Simulations, WORLD SCIENTIFIC, LERICI, Villa Marigola, 1998, pp. 385–404, http://dx.doi.org/10.1142/9789812839664_0016, ISBN: 978-981-02-3498-0 978-981-283-966-4.
[55] G. Henkelman, H. Jónsson, Improved tangent estimate in the nudged elastic band method for finding minimum energy paths and saddle points, J. Chem. Phys. 113 (22) (2000) 9978–9985, http://dx.doi.org/10.1063/1.1323224, (ISSN: 0021-9606, 1089-7690).
[56] C. Chen, mep, 2019, URL https://pypi.org/project/mep/.
[57] G. Henkelman, B.P. Uberuaga, H. Jónsson, A climbing image nudged elastic band method for finding saddle points and minimum energy paths, J. Chem. Phys. 113 (22) (2000) 9901–9904, http://dx.doi.org/10.1063/1.1329672, (ISSN: 0021-9606, 1089-7690).